Research on photodetdctors based on zinc-doped tin-lead perovskite quantum dots

Chenguang Shen(申晨光), Mengwei Chen(陈梦苇), Wei Huang(黄为), Zhaoyang Liu(刘朝阳), Yingping Yang(杨应平)

Citation: Chin. Phys. B. 35, 108502 (2026). DOI: 10.1088/1674-1056/ae2111 | CSTR: 32038.14.CPB.ae2111
http://cpb.iphy.ac.cn; http://iopscience.iop.org/cpb

What follows is a list of articles you may be interested in

Surface plasmons regulate photon absorbance, photo response and carrier injection in Ga_2O_3 photodetectors

Zhi-Kang Song(宋志康), Xiang-Xi Meng(孟祥熙), Pu-Yang Gao(高溥阳), Jia-Han Zhang(张嘉汉), Zeng Liu(刘增)

Chin. Phys. B. 35, 088501 (2026). DOI: 10.1088/1674-1056/ae5f07 | CSTR: 32038.14.CPB.ae5f07

Enhanced thermal stability of OLEDs based on an organic n–p heterojunction and its derivative

Wei Shi(施薇), Wei Zhao(赵微), Bingjia Zhao(赵冰佳), Yangyang Zhu(朱杨洋), Yang Lin(林洋), Yachen Xu(徐亚晨), Weixia Lan(兰伟霞), Bin Wei(魏斌)

Chin. Phys. B. 35, 038502 (2026). DOI: 10.1088/1674-1056/adfdc8 | CSTR: 32038.14.CPB.adfdc8

Strong enhancement of spin–orbit torques and perpendicular magnetic anisotropy in $[Pt_{0.75}Ti_{0.25}/Co–Ni\ multilayer/Ta]_n$ superlattices

Xiaomiao Yin(阴小苗), Zhengxiao Li(李政霄), Jun Kang(康俊), Changmin Xiong(熊昌民), Lijun Zhu(朱礼军)

Chin. Phys. B. 35, 018502 (2026). DOI: 10.1088/1674-1056/ae1c26 | CSTR: 32038.14.CPB.ae1c26

Modulation of exchange bias in Py/IrMn films by surface acoustic waves

Jie Dong(董洁), Shuai Mi(米帅), Meihong Liu(刘美宏), Huiliang Wu(吴辉亮), Jinxuan Shi(石金暄), Huifang Qiao(乔慧芳), Qian Zhao(赵乾), Teng-Fei Zhang(张腾飞), Chenbo Zhao(赵晨博), Jianbo Wang(王建波), Qingfang Liu(刘青芳)

Chin. Phys. B. 34, 088502 (2025). DOI: 10.1088/1674-1056/adce99 | CSTR: 32038.14.CPB.adce99

Investigation of degradation and recovery characteristics of NBTI in 28-nm high-*k* metal gate process

Wei-Tai Gong(巩伟泰), Yan Li(李闫), Ya-Bin Sun(孙亚宾), Yan-Ling Shi(石艳玲), Xiao-Jin Li(李小进)

Chin. Phys. B. 32, 128502 (2023). DOI: 10.1088/1674-1056/ace034

Research on photodetdctors based on zinc-doped tin-lead perovskite quantum dots

Chenguang Shen(申晨光), Mengwei Chen(陈梦苇)[†], Wei Huang(黄为), Zhaoyang Liu(刘朝阳), and Yingping Yang(杨应平)[‡]

Department of Physics, Wuhan University of Technology, Wuhan 430070, *China*

(Received 9 September 2025; revised manuscript received 31 October 2025; accepted manuscript online 19 November 2025)

The problems of Sn^{2+} being easily oxidized and the limited water–oxygen stability of Sn^{2+}-doped $CsPbBr_2I$ quantum dots (QDs) have hindered the further advancement of optoelectronic devices based on these materials, representing a key challenge in the field. In this study, we employed a double-doping strategy to prepare Sn–Zn:$CsPbBr_2I$ QDs. The incorporation of Zn^{2+} effectively contracts the crystal lattice and blocks oxygen diffusion pathways, thereby suppressing the oxidation of Sn^{2+}, which was confirmed by x-ray diffraction testing. Furthermore, the introduction of Zn^{2+} enhances the optical performance of the QDs. At an optimal Pb/Sn/Zn molar ratio of 0.85/0.10/0.05, the photoluminescence intensity increased by 78% compared with that of $CsPbBr_2I$ QDs. Additionally, the photodetector fabricated with Sn–Zn:$CsPbBr_2I$ QDs exhibited a responsivity of 0.44 A/W and a specific detectivity of 1.42×10^{13} Jones, outperforming the $CsPbBr_2I$ QD-based device (0.38 A/W and 6.07×10^{12} Jones). This work offers a new approach to enhancing the stability of Sn:$CsPbBr_2I$ QDs and supports the development of low-toxicity and high-performance optoelectronic devices.

Keywords: $CsPbBr_2I$ QDs, Sn^{2+} doping, Zn^{2+} doping, stability, photoelectric detector

PACS: 85.60.Gz, 78.67.Hc, 85.60.Bt

DOI: 10.1088/1674-1056/ae2111 **CSTR:** 32038.14.CPB.ae2111

1. Introduction

In recent years, all-inorganic perovskite quantum dots (PQDs), specifically $CsPbX_3$ (X = Cl, Br, I), have demonstrated great potential for optoelectronic applications owing to their high photoluminescence quantum yield, tunable emission wavelengths and narrow emission linewidths.[1–4] Adjusting the halide composition allows precise control over the band gap and luminescence properties of these quantum dots (QDs).[5,6] However, mixed-halide PQDs suffer from limited stability due to increased defect density, enhanced halide ion migration and structural thermodynamic instability,[7–10] which hinders their practical use. Additionally, the toxicity of lead remains a significant concern. Doping engineering has emerged as a promising approach to reduce lead content and improve both bulk and surface stability of perovskite materials.[11–13] Various elements such as Mn,[14,15] Sn,[16] Cu,[17] Fe,[18] Ge[19] and Ni[20] have been explored as dopants. Sn^{2+} is particularly attractive due to its similar ionic radius to Pb^{2+}, allowing effective substitution in the perovskite lattice. However, Sn^{2+} is prone to oxidation into Sn^{4+}, which leads to structural defects and Sn vacancies.[21,22] These defects speed up the formation of antisite defects, destroy the lattice's long-range order and reduce carrier mobility.[23,24] As a result, Sn^{2+} oxidation shortens the device's long-term stability and lowers its performance.[25]

To address Sn-related defects, surface treatments and additives have been investigated. For example, Mahmoudi *et al.*[26] incorporated reduced graphene oxide (rGO) to form a mixed organic cationic tin halide perovskite/graphene-tin QDs photoactive complex ($FA_xMA_{1-x}SnI_3$/rGO-Sn QDs), which improved light absorption and charge transport and reduced oxidation. However, the experimental operation is complex and involves the risk of converting Sn^{4+} and Sn^{2+} salts to Sn. Joy *et al.*[27] introduced SnX_2 as an additive into $FASnI_3$, serving as both a reducing agent and a Sn^{2+} source, which significantly improved the stability of $FASnI_3$. However, excess SnX_2 tends to aggregate at grain boundaries, destroying the film morphology. In contrast, co-doping with small-radius divalent ions such as Zn^{2+} offers a compelling alternative. Zn^{2+} incorporation can compress the lattice, suppress oxygen diffusion, passivate Pb^{2+} vacancies and mitigate deep-level defects, effectively inhibiting Sn^{2+} oxidation and enhancing the optical properties and stability of QDs.[28] Nevertheless, systematic studies on B-site co-doping strategies for suppressing Sn^{2+} oxidation are still scarce. To fully realize this strategy's potential for practical use, it is crucial to conduct a thorough investigation.

In our previous work,[29] we found that $CsPbBr_2I$ QDs exhibit optimal absorption, and photodetectors based on $CsPbBr_2I$/$CsPbBr_3$ QD heterostructures showed superior performance. Here, we use a double-doping strategy to syn-

[†]Corresponding author. E-mail: mengwei.chen@whut.edu.cn

[‡]Corresponding author. E-mail: ypyang@whut.edu.cn

© 2026 Chinese Physical Society and IOP Publishing Ltd. All rights, including for text and data mining, AI training, and similar technologies, are reserved.

thesize Sn–Zn:$CsPbBr_2I$ QDs (the molar ratio of Pb/Sn/Zn is 0.85/0.10/0.05). These QDs display enhanced optical performance and stability compared with $CsPbBr_2I$ QDs. After exposure to deionized water, the photoluminescence (PL) intensity of Sn–Zn:$CsPbBr_2I$ QDs retained 76.75% of its initial value, significantly higher than the 38.59% observed for Sn:$CsPbBr_2I$ QDs (the molar ratio of Pb/Sn is 0.90/0.10).

We fabricated hole-transport-layer-free photodetectors with a vertical structure: FTO/dense TiO_2 layer (c-TiO_2)/mesoporous TiO_2 layer (m-TiO_2)/QD photosensitive layer/carbon (C), using Sn–Zn:$CsPbBr_2I$ QDs as the photosensitive layer. Compared with the original device (with a photosensitive layer of $CsPbBr_2I$ QDs), the photocurrent increased by 15.62% (from 7.17×10^{-6} A to 8.29×10^{-6} A) and the dark current decreased (from 5.30×10^{-10} A to 1.51×10^{-10} A). Moreover, the specific detectivity and responsivity increased by 133.9% and 15.8%, respectively. Under continuous 400 nm illumination for 650 s, the photoresponse remained at 98% of its initial value, far exceeding that of the original device.

2. Experiment

2.1. Materials

Lead bromide ($PbBr_2$, 99.9%), cesium carbonate (Cs_2CO_3, 99.9%), tin bromide ($SnBr_2$, 99%), zinc bromide ($ZnBr_2$, 99%), octadecene (ODE, $>$ 90%), trioctylphosphine (TOP, 90%), oleylamine (OAM, 80%–90%), oleic acid (OA, $\geq$ 99.8%) and methyl acetate (MeOAc, $\geq$ 98%) were purchased from Macklin (China). Lead iodide (PbI_2, 99.999%) was purchased from Xi'an Bath Solar Energy Technology Co., Ltd. *n*-Octane ($\geq$ 98%), *n*-hexane ($\geq$ 97%), isopropanol ($\geq$ 99.7%), acetone ($\geq$ 99.5%) and absolute ethanol (99.7%) were purchased from China National Pharmaceutical Chemical Reagents Co., Ltd. FTO was purchased from YouXuan Technology Co., Ltd. Titanium diisopropoxide diacetylacetone (75%) was purchased from Sigma-Aldrich (USA). Low-temperature carbon electrode paste and TiO_2 paste (30 NRD) were purchased from Shanghai MaterWin New Materials Co., Ltd. The above materials were used directly without further treatment.

2.2. Preparation of QDs

In this study, QDs were synthesized using a one-pot method, with reproducibility confirmed through multiple experiments. The detailed procedures are described below. For the preparation of $CsPbBr_2I$ QDs, the following reagents were weighed inside a glove box and placed into a three-necked flask: 0.559 mmol $PbBr_2$, 0.2795 mmol PbI_2 and 0.135 mmol Cs_2CO_3. Then, 20 mL of ODE, 2 mL of OAM, 2 mL of TOP and 2 mL of OA were added sequentially. The mixture was stirred at 120 °C for 30 min. For Sn:$CsPbBr_2I$, Sn–Zn:$CsPbBr_2I$ and Zn:$CsPbBr_2I$ QDs, varying molar amounts of $SnBr_2$ and $ZnBr_2$ were introduced while proportionally reducing the quantity of $PbBr_2$, maintaining a total molar content of 0.8385 mmol. All other materials and conditions remained identical to the procedure above. After the heating and stirring step, the reaction mixture was rapidly cooled to room temperature to obtain the crude solution. Purification was performed by adding an equal volume of methyl acetate to the crude solution, followed by centrifugation at 10000 rpm for 5 min. The supernatant was discarded. The precipitate was redispersed in a mixture of *n*-hexane and methyl acetate (volume ratio 1:2, total volume 15 mL), and the centrifugation step was repeated. Finally, 5 mL of *n*-hexane was added and the solution was centrifuged at 3000 rpm for 5 min. The resulting supernatant was collected and evaporated to dryness with *n*-octane.

2.3. Preparation of the devices

In this study, QD photodetectors were fabricated via spin coating, with reproducibility confirmed through multiple experiments. The FTO glass substrate was ultrasonically cleaned in deionized water, isopropanol, acetone and anhydrous ethanol for 30 min, respectively, then stored in anhydrous ethanol. The m-TiO_2 precursor solution was prepared by mixing TiO_2 and ethanol in a 1:5 mass ratio for 24 h, while the c-TiO_2 precursor was made by mixing 0.1 mL diisopropyl alcohol diacetylacetone titanium with 1.9 mL ethanol for 30 min. The spin-coating preparation of the device required ultraviolet ozone cleaning of the cleaned FTO glass substrate for 20 min, and the c-TiO_2 precursor solution was spin-coated on it. The rotation speed and time were 4000 rpm and 30 s, respectively, followed by annealing at 150 °C for 10 min. This step was repeated, then the layer was annealed at 500 °C for 30 min and cooled to room temperature. The m-TiO_2 layer was deposited by spin-coating its precursor at 3500 rpm for 20 s, then annealing at 150 °C for 10 min and 500 °C for 30 min before cooling. The QD *n*-octane solution was spin-coated on the electron transport layer at 1000 rpm for 20 s, annealed at 80 °C for 10 min and cooled to form the photosensitive layer. Finally, a carbon electrode with an area of 0.04 cm^2 was screen-printed onto the photosensitive layer and dried at 100 °C for 10 min.

2.4. Characterization

Transmission electron microscope (TEM) imaging was done with a field emission high-resolution transmission electron microscope (JEM-2100F, JEOL, Japan) at an accelerating voltage of 200 kV. The crystal structure of the QDs was measured by x-ray diffraction (XRD). The absorption properties of the QDs were measured with a UV–visible spectrophotometer (UV-2600, Shimadzu, Japan), and the PL properties were measured by steady-state PL spectroscopy (RF-6000, Shimadzu, Japan). X-ray photoelectron spectroscopy

(XPS) of the QDs was performed with an ESCALAB 250 Xi (Thermo Fisher Scientific, USA). The cross-sectional image of the photodetector was measured with a field emission scanning electron microscope (SEM; JSM-7500F, JEOL, Japan). Light with different wavelengths and powers was provided by a monochromatic tunable light source (CME-OPS1000, Microenergy, China). Time-resolved photoluminescence (TRPL) was measured with a spectrofluorometer (FS5, Edinburgh Instruments, UK). The performance of the device was measured with a Keithley 4200 semiconductor characterization system.

3. Results and discussion

In this study, $CsPbBr_2I$ QDs were synthesized in colloidal form via a one-pot method at 120 °C. Figure 1 shows their TEM morphology, with an inset presenting a photograph of the corresponding colloidal solution. TEM results show that the QDs are uniformly sized and well dispersed in *n*-hexane. The TEM images of Sn:$CsPbBr_2I$ QDs and Sn–Zn:$CsPbBr_2I$ QDs are shown in Figs. S1(b) and S1(c). The particle sizes of the QDs are as follows: $CsPbBr_2I$ 10.06853 nm, Sn:$CsPbBr_2I$ 10.05917 nm, Sn–Zn:$CsPbBr_2I$ 10.05769 nm (Figs. S1(d)–S1(f)). The small amount of doping has little effect on the particle size of the QDs.

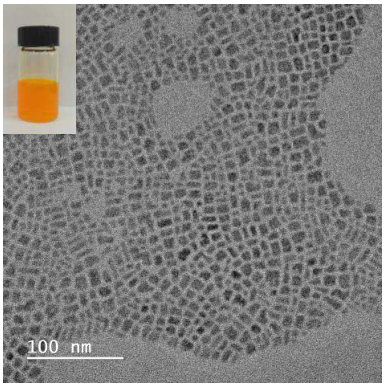

Fig. 1. TEM test diagram of $CsPbBr_2I$ QDs; the inset is a physical image.

We studied the effect of Sn^{2+} doping on the absorption and fluorescence of the QDs, with Pb/Sn molar ratios of 0.95/0.05, 0.90/0.10, and 0.85/0.15. Figures 2(a) and 2(b) show the absorption and PL spectra of Sn:$CsPbBr_2I$ QDs with Pb/Sn ratios of 1/0, 0.95/0.05, 0.90/0.10, and 0.85/0.15. The PL spectra were excited at 400 nm. Despite a slight decrease in absorption, the 0.90/0.10 sample exhibited a 48.28% higher fluorescence intensity than the $CsPbBr_2I$ QDs, indicating a significant enhancement. The 0.85/0.15 sample showed increased absorption, but its fluorescence intensity decreased significantly. This is likely due to excessive doping, which can introduce interstitial ions and defect sites, thereby reducing PL efficiency.[30] Therefore, the 0.90/0.10 sample was selected for further study and is hereafter referred to as Sn:$CsPbBr_2I$ QDs.

To enhance the structural stability of the QDs, Zn^{2+} was co-doped with Sn^{2+} due to its smaller ionic radius. In Figs. S2(a) and S2(b), we show the absorption and PL spectra of QDs with Pb/Sn/Zn molar ratios of 0.87/0.10/0.03, 0.85/0.10/0.05 and 0.82/0.10/0.08, respectively. Among them, the sample with a Pb/Sn/Zn molar ratio of 0.85/0.10/0.05 exhibits the best optical performance and was therefore selected for further experiments. These co-doped QDs are hereafter referred to as Sn–Zn:$CsPbBr_2I$ QDs. The XRD patterns of $CsPbBr_2I$, Sn:$CsPbBr_2I$, Zn:$CsPbBr_2I$ (with a Pb/Zn molar ratio of 0.95/0.05) and Sn–Zn:$CsPbBr_2I$ QDs are shown in Fig. 3(a). These results confirm that the cubic phase of the QDs is retained, regardless of single or co-doping. All the diffraction peaks remain consistent with the standard cubic phase $CsPbBr_3$ (PDF #54-0752). The PL and absorption spectra of $CsPbBr_2I$, Sn:$CsPbBr_2I$, Zn:$CsPbBr_2I$ and Sn–Zn:$CsPbBr_2I$ QDs are presented in Figs. 3(b) and 3(c), respectively. Although Zn^{2+} doping alone leads to the strongest absorption, the significant decrease in fluorescence intensity must also be considered. This is attributed to the difference in ionic radii between Pb^{2+} and Zn^{2+}, which introduces additional defects and promotes non-radiative recombination.[31] However, co-doping with Sn^{2+} helps alleviate this size mismatch. Compared with the Sn:$CsPbBr_2I$ QDs, the Sn–Zn:$CsPbBr_2I$ QDs exhibit significantly higher absorption and their PL intensity increased by 79.47%. The combination of Zn^{2+} and Sn^{2+} effectively suppresses the formation of deep-level defects, reduces non-radiative recombination centers and ultimately enhances the optical performance of the QDs.

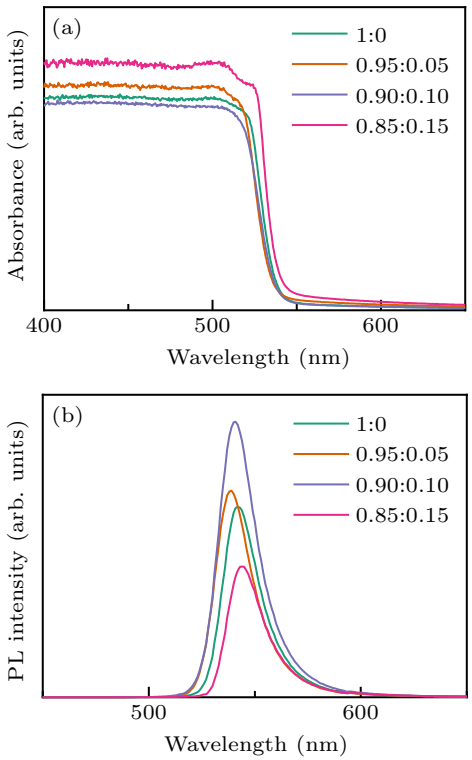

Fig. 2. (a) Absorption spectra and (b) PL spectra of Sn:$CsPbBr_2I$ QDs (1/0, 0.95/0.05, 0.90/0.10, 0.85/0.15).

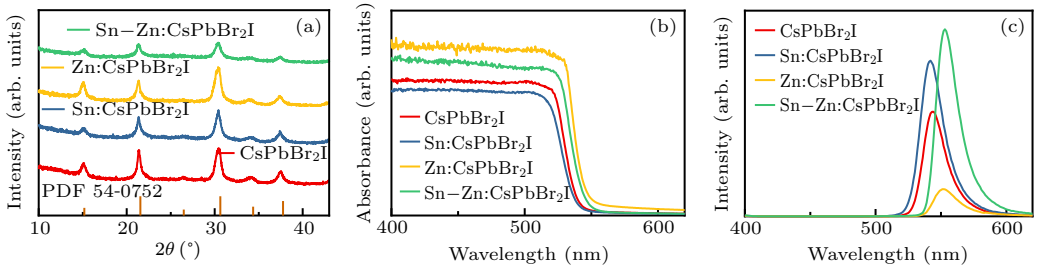

Fig. 3. (a) XRD test results, (b) absorption spectra and (c) PL spectra of $CsPbBr_2I$, Sn:$CsPbBr_2I$, Zn:$CsPbBr_2I$ and Sn–Zn:$CsPbBr_2I$ QDs.

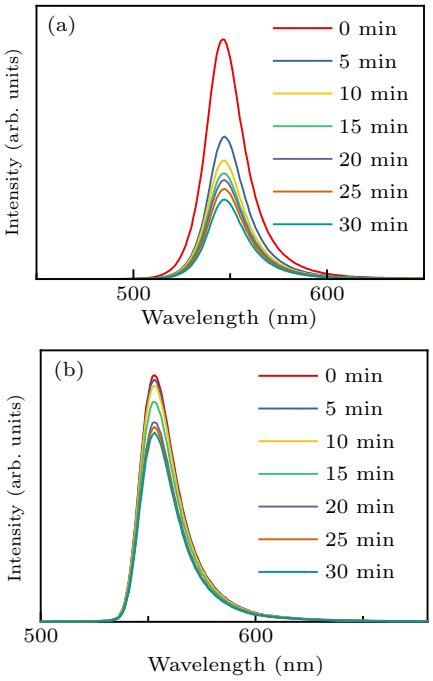

Fig. 4. PL spectra of QDs in deionized water: (a) Sn:$CsPbBr_2I$ QDs and (b) Sn–Zn:$CsPbBr_2I$ QDs.

To evaluate the effect of doping on QD stability, we added deionized water corresponding to 3% of the total volume to colloidal solutions of Sn:$CsPbBr_2I$ and Sn–Zn:$CsPbBr_2I$ QDs. PL measurements were taken every 5 min. After 30 min the results stabilized under a constant test wavelength of 400 nm. As shown in Figs. 4(a) and 4(b), the PL intensity of Sn–Zn:$CsPbBr_2I$ QDs retained 76.75% of its original value in deionized water, significantly higher than that of Sn:$CsPbBr_2I$ QDs (38.59%). This result demonstrates that the Sn–Zn dual-doping strategy markedly enhanced the structural stability and environmental resistance (against moisture and oxygen) of the QDs, thereby significantly improving the retention of their optical performance under humid conditions.

We also used XRD to study Sn:$CsPbBr_2I$ and Sn–Zn:$CsPbBr_2I$ QDs after their exposure to air, to evaluate their structural stability under these conditions. Films of Sn:$CsPbBr_2I$ and Sn–Zn:$CsPbBr_2I$ QDs were prepared on glass substrates and stored in ambient air. As shown in Figs. 5(a) and 5(b), both types of QDs initially exhibited a clear cubic structure, but partially transformed into the orthorhombic phase after 120 h. Sn:$CsPbBr_2I$ QDs show more impurity peaks between 20° and 30° than Sn–Zn:$CsPbBr_2I$, consistent with the $PbSnO_3$ phase (PDF #17-0607). The addition of Zn^{2+} helps inhibit the oxidation of Sn^{2+} to Sn^{4+}.

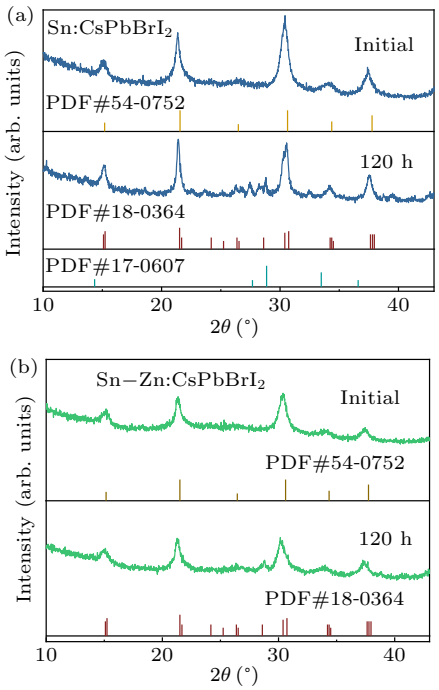

Fig. 5. Comparison of the XRD stability of QD films before and after storage in air for 120 h: (a) Sn:$CsPbBr_2I$ QDs and (b) Sn–Zn:$CsPbBr_2I$ QDs.

XPS was used to compare the elemental binding energies of Sn:$CsPbBr_2I$ and Sn–Zn:$CsPbBr_2I$ QDs to understand the enhanced stability of the co-doped material. High-resolution spectra of Cs $3d_{5/2}$, Pb $4f_{7/2}$, Br $3d_{5/2}$, Br $3d_{3/2}$, I $3d_{5/2}$, and I $3d_{3/2}$ are presented in Figs. 6(a)–6(d). After Zn^{2+} doping, the Cs $3d_{5/2}$ peak position remains unchanged, whereas those of I, Pb, and Br all shift slightly toward higher binding energy. The binding energy shifts for Pb $4f_{7/2}$ and Pb $4f_{5/2}$ were 0.20 eV and 0.29 eV, those for Br $3d_{5/2}$ and Br $3d_{3/2}$ were 0.21 eV and 0.18 eV, and those for I $3d_{5/2}$ and I $3d_{3/2}$ were 0.11 eV and 0.14 eV. These consistent shifts suggest that Zn^{2+} doping enhances the chemical interaction between Pb^{2+} and halide ions. As shown in Fig. 6(e), the interaction energies for Sn:$CsPbBr_2I$ and Sn–Zn:$CsPbBr_2I$ QDs were calculated to be −82.147 eV and −133.837 eV, respectively. The stronger chemical bonding inhibits ion diffusion and dissociation, reduces internal defects, and ultimately improves the photoelectric performance of the QDs.

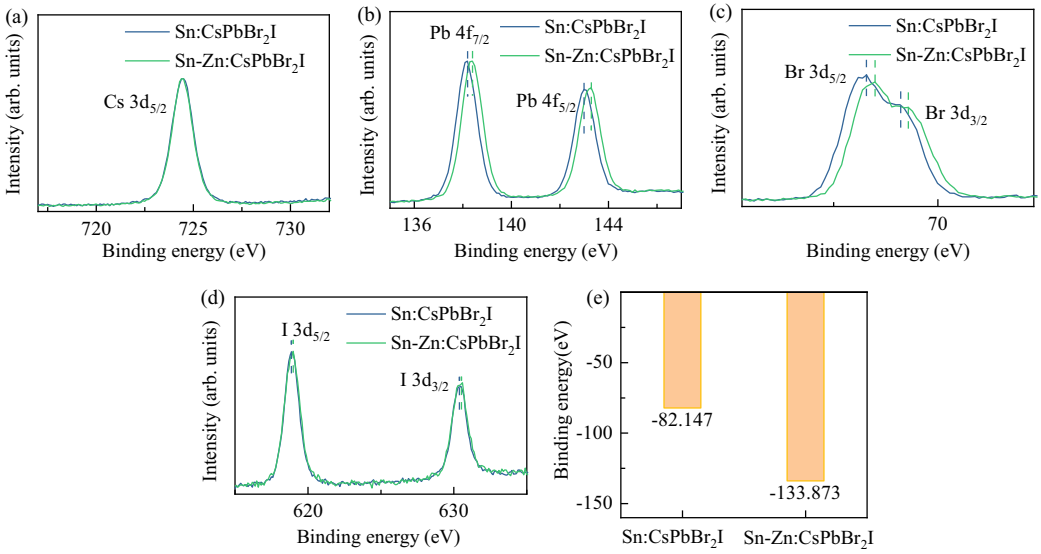

Fig. 6. XPS high-resolution spectra of different elements in Sn:CsPbBr$_2$I and Sn–Zn:CsPbBr$_2$I QDs: (a) Cs, (b) Pb, (c) Br and (d) I. (e) The results of interaction energy calculation for Sn:CsPbBr$_2$I and Sn–Zn:CsPbBr$_2$I QDs.

The TRPL spectra in Figs. S3(a) and S3(b) demonstrate a longer fluorescence lifetime for the Sn–Zn:CsPbBr$_2$I QDs (16.45 ns) than for the Sn:CsPbBr$_2$I QDs (13.21 ns) (the structure is ordinary glass/QDs). This enhancement is due to effective lattice passivation by Sn^{2+} and Zn^{2+} co-doping, which suppresses defect-mediated non-radiative recombination. These findings confirm that the Sn–Zn:CsPbBr$_2$I QD film possesses superior crystallinity and fewer defects, which paves the way for high-performance photodetectors.

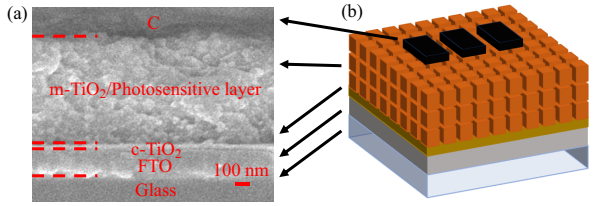

Fig. 7. (a) SEM scanning image of the cross-section of the device. (b) Schematic diagram of the device hierarchical structure.

CsPbBr$_2$I QDs, Sn:CsPbBr$_2$I, Zn:CsPbBr$_2$I, and Sn–Zn:CsPbBr$_2$I were used to fabricate hole-transport-layer-free photodetectors in a vertical structure. As shown in the cross-sectional SEM image in Fig. 7(a), the device consists of an FTO/c-TiO$_2$/m-TiO$_2$/QD photosensitive layer/C structure, with clear stratification and no visible cracks. The c-TiO$_2$ layer is approximately 50 nm thick, while the combined m-TiO$_2$ and QD photosensitive layer has a total thickness of about 750 nm. Thanks to its porous structure, the m-TiO$_2$ layer not only promotes electron transport but also provides ample space for infiltration of QDs, thereby enhancing both carrier transport efficiency and light absorption. A schematic diagram of the device layout is presented in Fig. 7(b).

The photoelectric performance of the devices was evaluated to study the effect of double-doping on the QD-based photodetectors. The photocurrents and dark currents of CsPbBr$_2$I, Sn:CsPbBr$_2$I, Zn:CsPbBr$_2$I and Sn–Zn:CsPbBr$_2$I QDs are shown in Figs. 8(a) and 8(b), respectively. QD devices were measured at 400 nm illumination and 0 V bias. The results indicate that the double-doped device exhibits the best performance. Compared with the CsPbBr$_2$I QD detector, its photocurrent increased by 15.62%, from 7.17×10^{-6} A to 8.29×10^{-6} A. Meanwhile, the dark current decreased by 71.51%, from 5.30×10^{-10} A to 1.51×10^{-10} A. In contrast, single doping with either Sn^{2+} or Zn^{2+} has a limited effect on device performance. In fact, Zn^{2+} doping alone even reduces the photocurrent, which can be attributed to the significantly

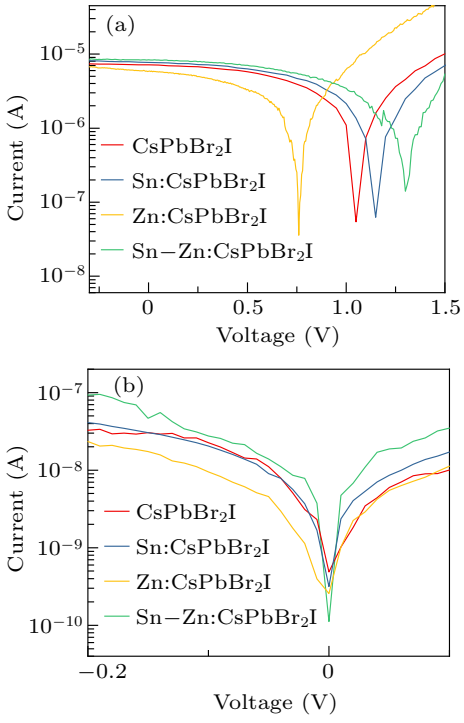

Fig. 8. (a) Photocurrent curves (0 V bias, 400 nm light) and (b) dark current curves of CsPbBr$_2$I, Sn:CsPbBr$_2$I, Zn:CsPbBr$_2$I and Sn–Zn:CsPbBr$_2$I QD photodetectors.

lower PL intensity of Zn:$CsPbBr_2I$ QDs. A lower PL intensity indicates a higher non-radiative recombination rate. Since non-radiative recombination consumes a large portion of the photogenerated carriers, it ultimately suppresses photocurrent generation.

Box plots of the photocurrent and dark current of the QD devices are shown in Figs. 9(a) and 9(b). Based on these results, the responsivity and specific detectivity of the devices were calculated using

$$R = \frac{I_{\text{light}} - I_{\text{dark}}}{P_{\text{in}} S}, \tag{1}$$

$$D^* = \frac{R\sqrt{S}}{\sqrt{2eI_{\text{dark}}}}. \tag{2}$$

Here, R represents responsivity (in A/W), I_{light} and I_{dark} are the photocurrent and dark current, P_{in} is the incident light power density, S is the effective device area, D^* is the specific detectivity [in $\text{cm}\cdot\text{Hz}^{1/2}\cdot\text{W}^{-1}$ (Jones)] and e is the elementary charge. The calculated results are shown in Figs. 9(c) and 9(d). The average responsivity values of $CsPbBr_2I$, Sn:$CsPbBr_2I$, Zn:$CsPbBr_2I$ and Sn–Zn:$CsPbBr_2I$ QDs are 0.38 A/W, 0.41 A/W, 0.31 A/W and 0.44 A/W, while the average specific detectivity values are 6.07×10^{12} Jones, 8.15×10^{12} Jones, 6.12×10^{12} Jones and 1.42×10^{13} Jones, respectively. Compared with the $CsPbBr_2I$ QD device, the Sn–Zn:$CsPbBr_2I$ device shows a 15.79% higher responsivity and a 133.94% higher specific detectivity.

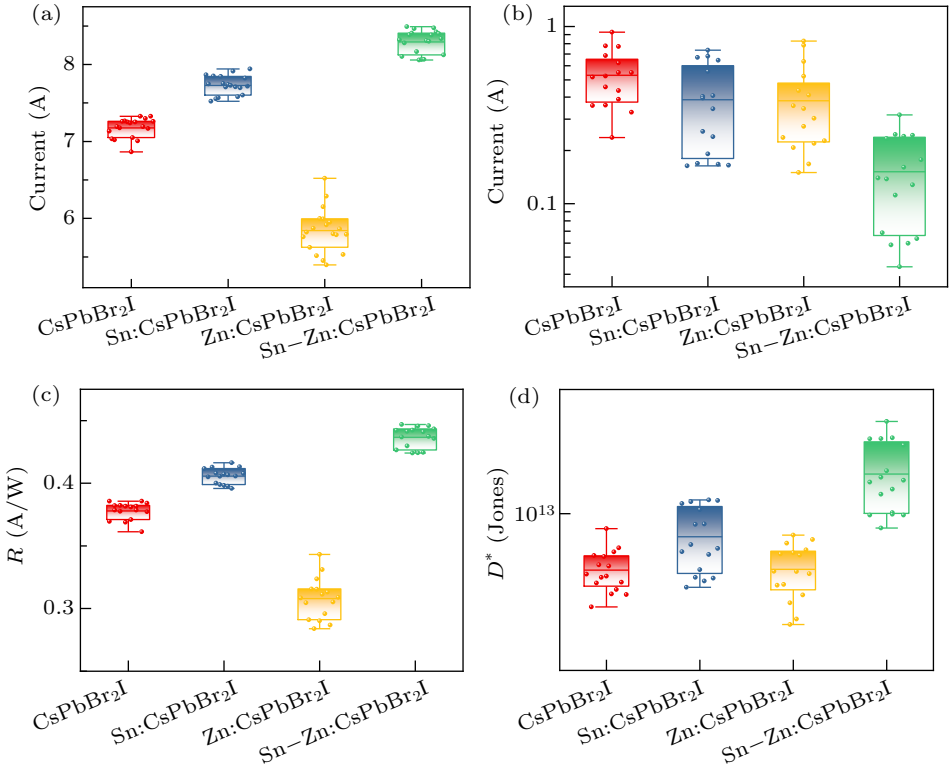

Fig. 9. Photoelectric performance box line statistics for $CsPbBr_2I$, Sn:$CsPbBr_2I$, Zn:$CsPbBr_2I$ and Sn–Zn:$CsPbBr_2I$ QD photodetectors (0 V bias, 400 nm illumination): (a) photocurrent, (b) dark current, (c) responsivity and (d) specific detectivity.

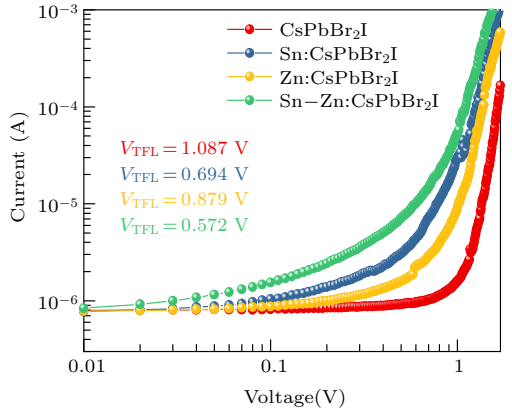

Fig. 10. SCLC test curves of $CsPbBr_2I$, Sn:$CsPbBr_2I$, Zn:$CsPbBr_2I$ and Sn–Zn:$CsPbBr_2I$ QDs.

The defect properties of the QD films were evaluated using the space charge limited current (SCLC) method. As shown in Fig. 10, the trap-filling limit voltage (V_{TFL}) values for the $CsPbBr_2I$, Sn:$CsPbBr_2I$, Zn:$CsPbBr_2I$ and Sn–Zn:$CsPbBr_2I$ QD films are 1.087 V, 0.694 V, 0.879 V and 0.572 V, respectively. The defect density (N_{t}) of each film was then calculated using

$$N_{\text{t}} = \frac{2\varepsilon_0\varepsilon_{\text{r}}V_{\text{TFL}}}{qL^2}, \tag{3}$$

where ε is the vacuum permittivity, ε_{r} is the relative dielectric constant of the all-inorganic perovskite,[32] q is the elementary charge and L is the thickness of the film. The calculated defect state densities for the $CsPbBr_2I$, Sn:$CsPbBr_2I$, Zn:$CsPbBr_2I$ and Sn–Zn:$CsPbBr_2I$ QD films are 3.394×10^{15} cm^{-3}, 2.167×10^{15} cm^{-3}, 2.745×10^{15} cm^{-3} and 1.786×10^{15} cm^{-3},

respectively. The Sn–Zn:CsPbBr$_2$I QDs exhibit the lowest defect state density. This is attributed to the co-doping of Sn^{2+} and Zn^{2+}, which effectively occupy the Pb^{2+} vacancies formed during synthesis. This occupation eliminates deep-level defects, thereby enhancing device performance.[33]

The above results confirm that Sn–Zn:CsPbBr$_2$I QDs possess superior stability to Sn:CsPbBr$_2$I QDs. To further compare their device performance, the response time curves of both types of QD-based photodetectors are shown in Figs. 11(a) and 11(b), where t_r represents the rise time and t_f represents the fall time. The rise time is defined as the time taken for the signal to increase from 10% to 90% of its maximum value, while the fall time is the time taken to decrease from 90% to 10% of its maximum value. The Sn:CsPbBr$_2$I QD detector has a rise time (green shaded area) of 48 ms and a fall time (brown shaded area) of 47 ms. In comparison, the Sn–Zn:CsPbBr$_2$I QD detector shows a faster response, with rise and fall times of 37 ms and 36 ms, respectively. These results indicate that the double-doped device responds more quickly to signal changes and exhibits higher sensitivity.

The light stability of the devices was tested over a period of nearly 650 s, as shown in Figs. 12(a)–12(f). The Sn–Zn:CsPbBr$_2$I QD device maintained a stable photoresponse with no attenuation, whereas the Sn:CsPbBr$_2$I QD device decayed to 90% of its initial value under prolonged illumination. This decline is attributed to increased recombination losses under continuous light exposure.

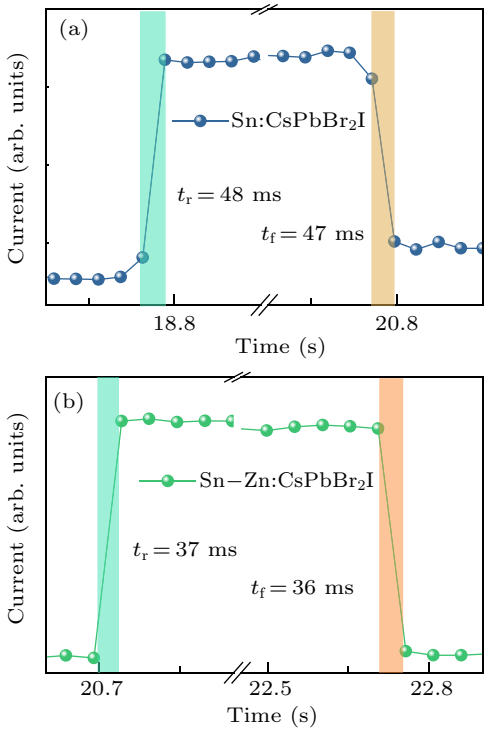

Fig. 11. Response time of QD photodetectors: (a) Sn:CsPbBr$_2$I QDs and (b) Sn–Zn:CsPbBr$_2$I QDs.

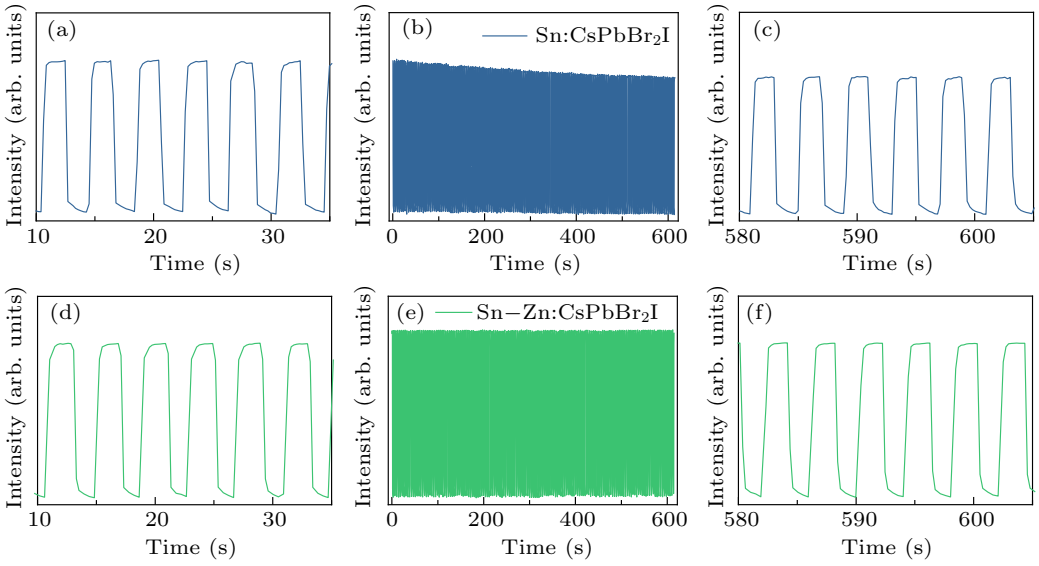

Fig. 12. The light on/off response characteristics of the photodetectors during the 650 s test cycle. (a)–(c) Sn:CsPbBr$_2$I QDs: (a) 10–35 s, (b) 0–650 s, (c) 580–650 s. (d)–(f) Sn–Zn:CsPbBr$_2$I QDs: (d) 10–35 s, (e) 0–650 s, (f) 580–650 s.

4. Conclusion

In summary, we successfully synthesized Sn^{2+} and Zn^{2+} co-doped CsPbBr$_2$I QDs. Both experimental and theoretical results demonstrate the superiority of this dual-doping approach in enhancing the optical properties and stability of the QDs. Theoretical calculations and XPS measurements confirm an increase in binding energy. XRD analysis reveals that Zn^{2+} doping effectively suppresses the oxidation of Sn^{2+} and improves the structural stability of the QDs. The photodetector based on double-doped QDs also exhibits excellent stability. The device can maintain 98% light response stability under continuous illumination at 400 nm wavelength for 650 s. In this study, we improved both the stability and optical properties of CsPbBr$_2$I QDs through a double-doping strategy. This approach significantly enhances the environmental tolerance of CsPbBr$_2$I QDs in optoelectronic devices, offering a new di-

rection for designing high-performance and long-lasting perovskite QD photodetectors.

Acknowledgement

The project supported the Fundamental Research Funds for the Central Universities of China (Grant No. 104972025KFYjc0086).

References

[1] Huang C Y, Li H C, Wu Y, Lin C H, Guan X W, Hu L, Kim J Y, Zhu X M, Zeng H B and Wu T 2023 *Nano-Micro Lett.* **15** 16
[2] Liu Z S, Wang Y, Zhao F, Li H H, Liu W Z, Shen W S, Duan H W, Wang Y K and Liao L S 2025 *Light. Sci. Appl.* **14** 35
[3] Jiang J X, Li R H, Liu D L, Xie H T, Zeng Q G and Li Y B 2023 *ACS Appl. Energy. Mater.* **6** 5378
[4] Shi J W, Kleinstein B C, Zhang X L, Zhao C Y, Zhang Y, Ling X F, Guo J J, Ko D H, Xu B M, Yuan J Y and Ma W L 2023 *Nano-Micro Lett.* **15** 163
[5] Wang R W, Zhao J Q, Ma J M, Lu C X, Yu Z S, Tu G L and Zhang J B 2024 *ACS Energy. Lett.* **9** 4699
[6] Feng Y F, Zhu M Y, Cao Q L, Li H J, Zhu X F, Lyu X Y, Dai X L, He H P and Ye Z Z 2024 *ACS Energy. Lett.* **9** 1125
[7] Zhou X, Zhang J B, Tong X, Sun Y B, Zhang H Y, Min Y G and Qian Y N 2022 *Adv. Opt. Mater.* **10** 2101517
[8] Lin Y L, Wu Z N, Mei E R, Yang J P, He Y, Xu Z B, Liang X J, Hu X G, Liu R W and Xiang W D 2025 *Appl. Surf. Sci.* **684** 161796
[9] Liu K L, Zhao J, Pan G C, Zhang H F, Zhu Y X, You W W, Gao H F and Mao Y L 2022 *Nanoscale* **14** 4263
[10] Sun Y B, Qi Q C, Zhou X, Min Y G and Qian Y N 2023 *Appl. Surf. Sci.* **638** 157970
[11] Hou L, Zhu Y H, Zhu J R, Gong Y Q and Li C Z 2020 *J. Mater. Chem. C* **8** 8502
[12] Yu H Q, Chen W J, Fang Z B, Ding L M, Cao B Q and Xiao Z G 2022 *Sci. Bull.* **67** 54
[13] Zhang L W, Chen Y B, Zheng Z M, Zhou Y, Li C, Li G, Ren B, Hu Z Q, Zhou H, Ren F Q, Ke W J and Fang G J 2025 *Adv. Funct. Mater.* **35** 2423450
[14] Zhang W H, Liu H, Qu Y T, Cui J S, Zhang W J, Shi T T and Wang H L 2024 *Adv. Mater.* **36** 2309193
[15] Chen M W, Huang W, Shen C G, Yang Y P and Shen J 2025 *Nanomaterials* **15** 444
[16] Yu H, Zhang X Z, Song L K, Li G, Wang Y C, Cao Y Z, Xu S, Zhang J S and Chen B J 2025 *Ceram. Int.* **51** 3934
[17] Mahmoudi T, Wang Y S, Im Y H and Hahn Y B 2025 *Mater. Today. Energy* **50** 101866
[18] Wu W, Zhao C Y, Hu M Y, Pan A Z, Xiong W and Chen Y H 2023 *Nanoscale* **15** 5705
[19] Sahamir S R, Kapil G, Bessho T, Segawa H, Shen Q and Hayase S 2024 *ACS Mater. Lett.* **6** 1241
[20] Kim H, Bae S R, Lee T H, Lee H, Kang H, Park S, Jang H W and Kim S Y 2021 *Adv. Funct. Mater.* **31** 2102770
[21] Liu F, Jiang J K, Zhang Y H, Ding C, Toyoda T, Hayase S, Wang R X, Tao S X and Shen Q 2020 *Angew. Chem. Int. Ed.* **59** 8421
[22] Li H, Gao Y, Hong X, Ke K H, Ye Z L, Zhang S W, Shi K F, Peng Z, Yan H, Tang M C, Yao Y W, Tang B Z, Wei G D and Kang F Y 2025 *InfoMat* **7** e12615
[23] Solari S F, Poon L N, Wörle M, Krumeich F, Li Y T, Chiu Y C and Shih C J 2022 *J. Am. Chem. Soc.* **144** 5864
[24] Yan D D, Mo Q H, Zhao S Y, Cai W S and Zang Z G 2021 *Nanoscale* **13** 9740
[25] Liu Z R, Wang G L, Kong L M, Wang J H, Wang Y Z, Du P, Wang L, Wang S, Rogach A L and Yang X Y 2025 *Nano Lett.* **25** 7061
[26] Mahmoudi T, Rho W Y, Kohan M, Im Y H, Mathur S and Hahn Y B 2021 *Nano Energy* **90** 106495
[27] Joy S, Hossain T, Tichy A, Johnson S and Graham K R 2024 *J. Phys. Chem. Lett.* **15** 3851
[28] Cao H, Zhang Z, Zhang M, Gu A, Yu H, Ban H, Sun Q, Shen Y, Zhang X L, Zhu J and Wang M 2021 *Mater. Today. Physics* **21** 100513
[29] Shen C G, Chen M W, Huang W and Yang Y P 2025 *J. Semicond.* **46** 102801
[30] Song L, Zhang Q, Ullah S, Liu K N, Liu Y X and Dai J 2023 *J. Mater. Chem. C* **11** 4526
[31] Zhuang B, Liu Y, Yuan S, Huang H, Chen J K and Chen D Q 2019 *Nanoscale* **11** 15010
[32] Liao S N, Chen M W, Li J, Zhang R and Yang Y P 2024 *J. Mater. Sci.: Mater. Electron.* **35** 715
[33] Varnakavi N, Gupta K, Lee K, Yang J, Cha P R and Lee N 2023 *J. Mater. Chem. C* **11** 14248